J Infrared Milli Terahz Waves
DOI 10.1007/s10762-015-0239-4

Improving the Out-Coupling of a Metal-Metal Terahertz Frequency Quantum Cascade Laser Through Integration of a Hybrid Mode Section into the Waveguide

Tobias Fobbe[1,2] · Hanond Nong[1] · Rüdiger Schott[2] · Shovon Pal[1,2] · Sergej Markmann[1] · Negar Hekmat[1] · Jingxuan Zhu[3] · Yingjun Han[3] · Lianhe Li[3] · Paul Dean[3] · Edmund H. Linfield[3] · A. Giles Davies[3] · Andreas D. Wieck[2] · Nathan Jukam[1]

Received: 18 June 2015 / Accepted: 21 December 2015

Abstract A hybrid mode section is integrated into the end of the metal-metal waveguide of a terahertz (THz) frequency quantum cascade laser (QCL) by removing sub-wavelength portions of the top metal layer. This allows a hybrid mode to penetrate into the air, which reduces the effective index of the mode and improves the out-coupling performance at the facet. The transmission of the hybrid section is further increased by ensuring its length fulfills the criterion for constructive interference. These simple modifications to a 2.5-THz metal-metal QCL waveguide result in a significant increase in the output emission power. In addition, simulations show that further improvements in out-coupling efficiency can be achieved for lower frequencies with effective refractive indices close to the geometric mean of the indices of the metal-metal waveguide and air.

Keywords Terahertz · Hybrid waveguide · Metal-metal waveguide · Surface plasmon waveguide · Quantum cascade laser

✉ Tobias Fobbe
Tobias.Fobbe@rub.de

✉ Nathan Jukam
nathan.jukam@ruhr-uni-bochum.de

[1] AG Terahertz Spektroskopie und Technologie, Ruhr-Universität Bochum, D-44780 Bochum, Germany

[2] Lehrstuhl für Angewandte Festkörperphysik, Ruhr-Universität Bochum, D-44780 Bochum, Germany

[3] School of Electronic and Electrical Engineering, University of Leeds, Leeds LS2 9JT, UK

Published online: 06 January 2016

Terahertz (THz) quantum cascade lasers [1] (QCLs) attain the highest temperature performance [2] in metal-metal (MM) waveguides [3], in which the laser mode is completely confined in the active region by two metal layers. The dimensions of the mode in the growth direction are typically less than the wavelength. This results in a significant impedance mismatch at the interface that increases the reflection coefficient, and the probability that a THz photon is reabsorbed in the waveguide [4]. In addition, the THz radiation is strongly diffracted from what is essentially a sub-wavelength slit at the facet, which makes it difficult to collect and collimate the THz beam [5]. While the highest THz QCL temperature performances have been achieved in MM QCL waveguides, the highest emitted THz QCL powers [6–8] have been recorded with surface plasmon waveguides where a significant portion of the laser field resides outside the active region. The increased spatial extent of the surface plasmon mode leads to an improvement of both the out-coupling performance and the beam diffraction at the expense of a reduction in the confinement factor of the mode in the active region. This in turn reduces the maximum operating temperatures. Although active regions can be bonded together [9] to produce thicker MM waveguides for higher power emission, this requires a symmetric QCL active region design. As alternatives, several approaches have been employed to increase the out-coupling efficiency and improve the beam characteristic of MM waveguides. These include out-of-plane emission by using one-dimensional gratings [10–12] and two-dimensional photonic crystals [13], attaching objects such as silicon hemispherical lenses [14] and polymer waveguides [15] to the end facets of the QCL and using meta-materials [16, 17] and spoof-surface plasmon modes [18, 19]. Other strategies employ tapered horns [20–23], for which the penetration depth of the mode in air slowly increases from zero to a large value at the end of the waveguide. Furthermore, a hybrid waveguide was recently introduced [24] that allowed the mode to leak through a thin top metal layer into a low-index polymer. This offers a compromise between the high out-coupling efficiency of a surface plasmon waveguide and the large confinement factor of a MM waveguide.

In this work, we employ a simple modification to a MM waveguide that significantly increases the out-coupling efficiency. Narrow lines are etched into the top-metal contact of a MM waveguide with a period and width much less than the wavelength. These etched lines allow the mode to penetrate into the air and form a hybrid mode. In addition, the length of the hybrid section of the QCL cavity is chosen such that the emission wavelength experiences constructive interference from reflections at the air-hybrid and MM-hybrid boundaries.

These extremely simple modifications to the MM waveguide result in a significant improvement in the out-coupling efficiency that is demonstrated from measurements on a 2.5-THz QCL. In addition, finite difference time domain (FDTD) simulations from a commercial software package were used to investigate the out-coupling process in more detail and explore the full potential of the proposed concept.

The THz QCL used is based on a LO-phonon miniband active region design modified for nominal emission at 2.7 THz [25]. Variants of this design emitting at higher frequencies have set several THz QCL power records when processed into surface plasmon waveguides [7, 8]. In this study, THz QCLs are processed as MM waveguides with a 13-μm-thick active region, 95-μmridge width, and a length of 1.58 mm. Lines are milled through the 150-nm-thick top-metal layer using a focused ion beam (FIB) of Ga+ ions with an energy of 30 keV. Furthermore, 150 nm of the doped GaAs surface is milled to ensure that the n++ contact layer is removed. The period 2d (2 μm) is much less than the emission wavelength of the QCL in both air and in the MM waveguide, which allows the lines to be treated as an effective medium. As shown in Fig. 1, the hybrid section is immediately adjacent to the out-coupling facet. The

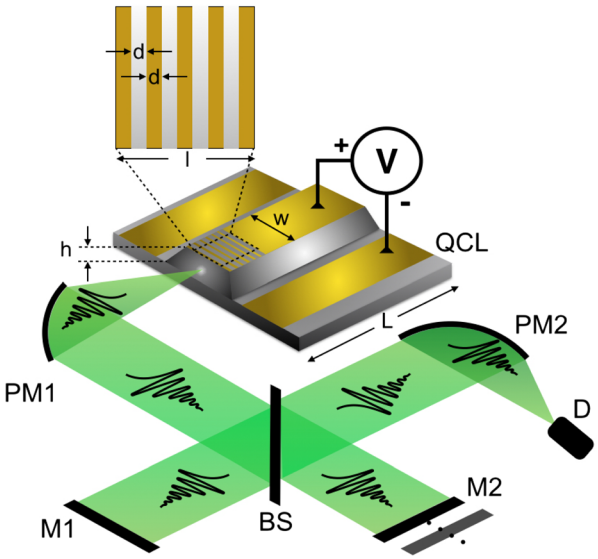

Fig. 1 Schematic diagram of the experimental arrangement, showing relevant dimensions of the metal-metal hybrid section (MMHS) waveguide. The length (L), height (h), and width (w) of the QCL are 1.58 mm, 13 μm, and 95 μm, respectively. The length of the hybrid section (l) is 38 μm. The distance between the metal lines (d) is 1 μm. Two parabolic mirrors PM1 and PM2, a beam splitter BS, a static mirror M1, and a movable mirror M2 form a Michelson interferometer that is used to detect the spectrum with a pyroelectric detector D

length of the hybrid section is 38 μm, which is only 2.5 % of the total length of the 1.58-mm waveguide. The metal-metal hybrid section (MMHS) waveguide and a reference MM waveguide (of identical dimensions) approximately 225 μm apart on the same wafer die were mounted on an Au-coated copper sub-mount. This allowed for consecutive measurements of the hybrid and reference samples in a helium flow cryostat. The cryostat can be positioned using large translation stages and micrometers which have a resolution of 10 μm. This enables the MMHS and MM QCLs to be placed at the same position for consecutive measurements.

All measurements were performed at a temperature of 10 K and in purged environment. In order to characterize the spectral emission of the QCL, a step-scan Michelson interferometer was employed as an Fourier transform spectrometer. The maximum scan length is 20 mm which corresponds to a frequency resolution of approximately 7.5 GHz. A high resistivity silicon wafer is used as a 45 ^{o} beam splitter. The THz radiation is collected with a 90 ^{o} off-axis parabolic mirror (focal length = 225 mm, diameter = 75 mm), sent through the interferometer, and then focused onto a pyroelectric detector via an additional and identical 90 ^{o} off-axis parabolic mirror. The QCLs are modulated at 10 kHz with a 10 % duty cycle for voltage-current measurements. For laser emission measurements, the 10-kHz modulation is further modulated with a duty cycle of 50 % at 10 Hz in order to match the maximum frequency response of the pyro-electric detector. The voltage versus current density and the output power of the QCLs are presented in Fig. 2a, with the output power recorded with a 5-mm pyroelectric detector placed approximately 40 mm away from the QCLs. Both the reference and the hybrid QCL reached laser threshold at a current density of approximately 530 A/ cm^2. At all current values, the emitted power of the MMHS waveguide is significantly greater than the reference MM waveguide. Specifically, at current densities of 590 A/cm^2 and 720 A/cm^2, indicated by the pink dashed lines in Fig. 2a, the power of the MMHS waveguide is approximately 2.9 times that of the MM waveguide. In addition, at a current density of 620 A/cm^2, just above the kink in the L-I curve, the ratio of the output powers is approximately 4.0. The QCL spectra at the current densities denoted by the pink dashed lines are presented in Fig. 2b–d. For low-current densities, the QCL emission is predominantly single mode, as

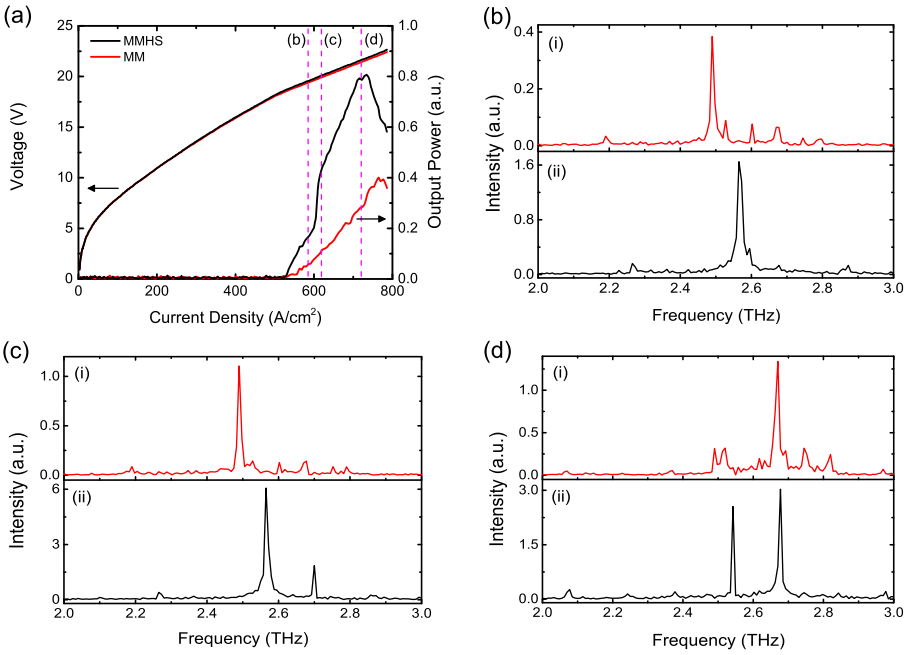

Fig. 2 **a** QCL output power and voltage as a function of current density for both the meta-lmetal hybrid section (MMHS) waveguide (*black*) with l = 38 μm and the metal-metal (MM) waveguide (*red*). The spectra from the MM (i—*red*) and MMHS (ii—*black*) QCL waveguides are shown for current densities of **b** 590 A/cm^2, **c** 620 A/cm^2, and **d** 720 A/cm^2

shown in Fig. 2b, with frequencies centered at 2.48 and 2.56 THz for MM and MMHS waveguides, respectively. At higher-current densities, the spectral emission of both QCLs shifts to higher frequencies. For the MM waveguide, QCL lasing takes place primarily at 2.7 THz, while the MMHS waveguide provides significant emission at the original 2.56-THz lasing mode in addition to providing a new mode at 2.7 THz. The significant emission observed near 2.5 THz can be attributed to the MMHS waveguide which is optimized for a frequency of 2.5 THz.

In order to complement the demonstration of the concept by the experiment, finite difference time domain (FDTD) simulations from a commercial software package were used to model the out-coupling of the two waveguides. In the simulations, both the MM and MMHS waveguides are placed on top of a GaAs substrate. Only the emission from one end of the QCL was modeled in the simulation. We thus neglect any fringes in the far-field that originate from the interference of the emission between the opposite facets [26]. The total efficiency, which is defined as the radiated power (integrated over all angles) divided by the input power, of the MMHS waveguide is calculated to be 2.2 times that obtained for the MM waveguide at a frequency of 2.5 THz. The calculated far-field distribution of the two waveguides is shown in Fig. 3 as a function of the azimuthal and polar angles θ and φ, respectively. In the normal direction of the waveguide (at $\theta = 0^{\circ}$ and $\varphi = 0^{\circ}$ in Fig. 3), the ratio of the intensity in the far-field emission between the MM and MMHS waveguides is 2.9. The increase in both the total radiative efficiency and the power in the far-field is due to the penetration of the mode into the air and the constructive interference between the ends of the hybrid section of the waveguide.

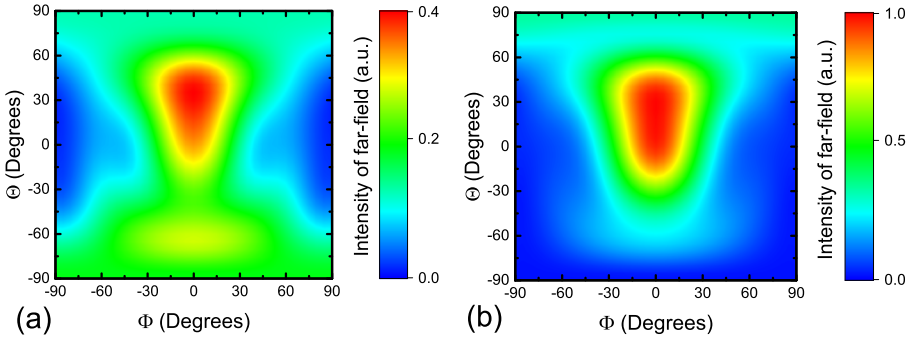

Fig. 3 Comparison of the simulated far-field emission profiles for **a** the metal-metal (MM) waveguide and **b** the metal-metal with hybrid section (MMHS) waveguide at a frequency of 2.5 THz. The length of the hybrid section (l in Fig. 1) of the MMHS waveguide is 38 μm. The direction normal to the QCL facet corresponds to $\varphi = 0°$ and $\theta = 0°$

This is illustrated in Fig. 4, which shows the absolute value of the electric field for two MMHS waveguides with different hybrid sections optimized for constructive (Fig. 4a) and destructive (Fig. 4b) interference. It is found that total efficiency is maximized for hybrid sections with lengths of

$$l = m\frac{c}{2fn_{eff}} \tag{1}$$

where m is an integer, f is the frequency, c is the speed of light in vacuum, and n_{eff} is the effective refractive index of the hybrid section (i.e., the component of the wave-vector in the propagation direction). The effective refractive index is defined as $n_{eff} = \frac{c\beta}{\omega}$ where ω is the angular frequency, and β is the propagation constant of the mode. A hybrid section with a length of $l = 38$ μm (as used in this study) corresponds to $m = 2$ at a frequency of 2.5 THz.

The propagation constant (and hence the effective refractive index) can be found by extending the length of the hybrid section in the simulations and determining the period of the mode in the propagation direction. The simulated dispersion relation is shown in Fig. 5a

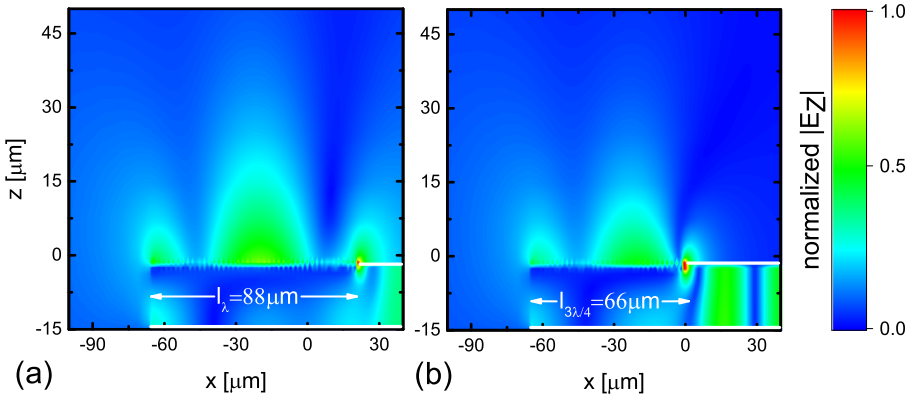

Fig. 4 The absolute value of the z-component of the electric field at a frequency of 1.7 THz of metal-metal (MM) with hybrid section (MMHS) QCL waveguides displaying **a** destructive and **b** constructive interference between the air-hybrid interface and the hybrid-MM interface. The length l of the hybrid section is 66 μm in (**a**) and 88 μm in (**b**). The *solid white lines* represent the metal boundaries of the waveguides

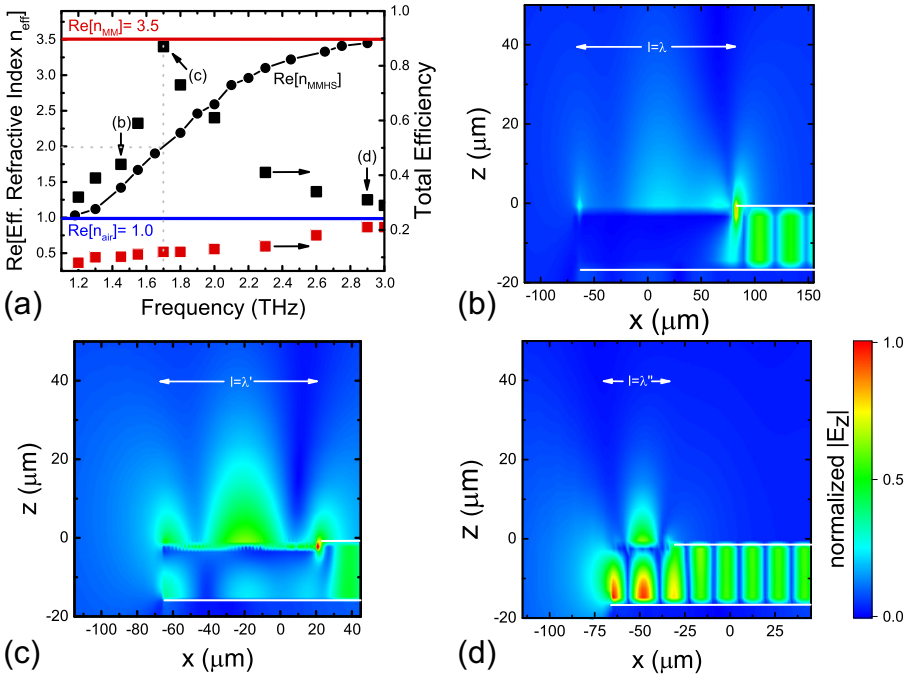

Fig. 5 **a** The dispersion relation of the effective index of the metal-metal with hybrid section (MMHS) waveguide (*black dots*) compared to the dispersion relation of the metal-metal (MM) waveguide (*red line*) and air (*blue line*). On the right y axis, the total efficiency is presented for the MMHS waveguide (*black squares*) compared to the total efficiency of the MM waveguide (*red squares*). The mode profile of the absolute value of the z-component in the x-z plane of the MMHS waveguide is shown for frequencies of **b** 1.45 THz, **c** 1.7 THz, and **d** 2.9 THz. In each (**b**), (**c**), and (**d**), the length of the hybrid sections, 146 μm, 88 μm, and 30 μm, respectively, is optimized for constructive interferences with $m = 2$ in Eq. (1)

(black dots). For high frequencies, the effective index approaches the MM waveguide index while for low frequencies it converges to 1. Interestingly, the effective refractive index of the

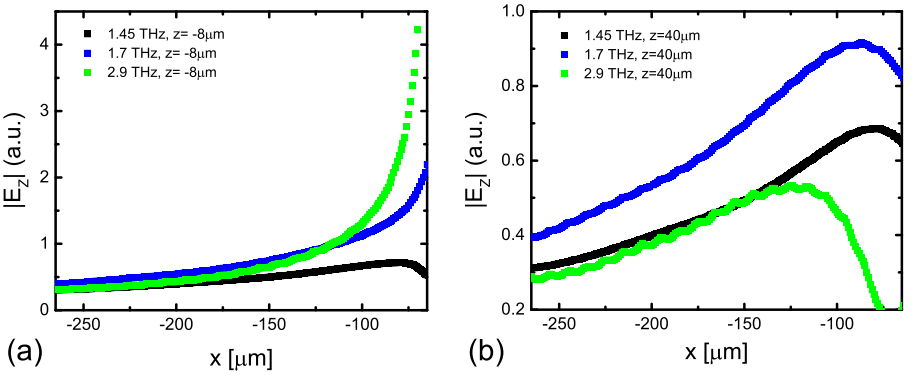

Fig. 6 Absolute value of the emitted electric field E_z as a function of propagation distance x according to Fig. 5. In **a,** the fast decay in the 2.9-THz case is attributed to the evanescent character due to the high index contrast at the hybrid-air interface. In **b**, the emission is displayed for a z-position above the laser, since the emission takes place predominantly at this area for the low refractive index cases

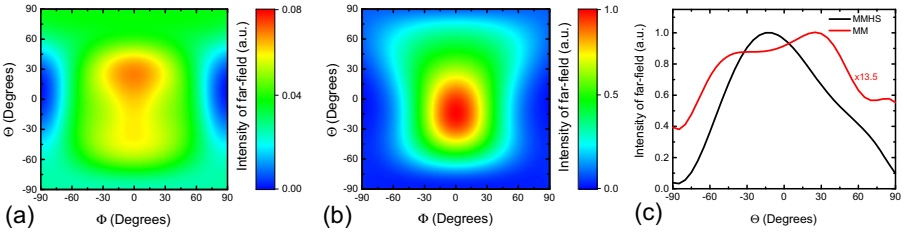

Fig. 7 Simulated far-field for a reflection optimized structure at a frequency of 1.7 THz and for a waveguide height of d = 13 μm for **a** the MM waveguide, **b** the MMHS waveguide, and **c** both waveguides at Φ = 0°. The far-field intensity at Φ = 0° and Θ = 0° is improved by factor of 14.2 and according to Fig. 5 about 87 total efficiency is achieved

hybrid waveguide (3.16) is only about 11 % less than that of the MM Waveguide (3.5). This suggests that if the frequency (and hence effective index) is decreased, the out-coupling efficiency can be further improved—provided that the length of the hybrid section is adjusted such that the criterion for constructive interference (Eq. (1)) is still satisfied. Indeed, as the frequency decreases, the total efficiency as shown in Fig. 5a (black dots) initially increases. The key role that the extension of the hybrid mode plays in improving the out-coupling efficiency is illustrated in Fig. 5b–d which shows the field distribution at 1.45 THz, 1.7 THz, and 2.9 THz for MMHS waveguides with hybrid section lengths that maximize constructive interference. As the frequencies decreases, the penetration depth of the mode into the air increases. This is expected since in general, the penetration depth of the mode in air is related to the effective index by $l_{eff} = \frac{\lambda}{2\pi\sqrt{(n_{eff}{}^2-1)}}$ [27]. The increase in the spatial extent of the mode decreases the spatial mismatch between the waveguide mode and the air modes at the hybrid-air interface which reduces its reflection coefficient. The total efficiency peaks at a frequency of 1.7 THz which has an effective index (n_{eff} = 2.0) that is close to the geometric mean of the MM waveguide and air. The decrease in the total efficiency for frequencies below 1.7 THz is due the increase in the reflection coefficient at the hybrid-MM boundary for lower frequencies. This can be seen in Fig. 5b (for a frequency of 1.45 THz) where the field strength at the MM-hybrid interface is greater than the hybrid-air interface. In contrast, the field distribution at the hybrid-air interface is greater than the MM-hybrid interface for frequencies above 1.7 THz as shown in Fig. 5d (for a frequency of 2.9 THz). Consequently, when the total efficiency is maximized near 1.7 THz, the strength of the field distribution at both boundaries is roughly equivalent.

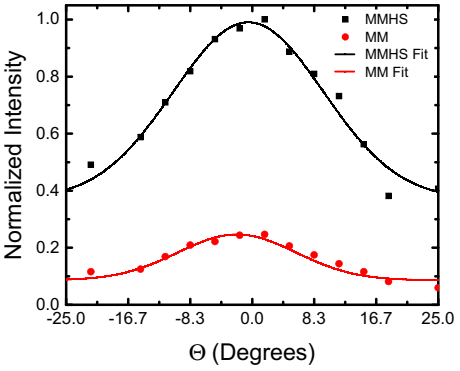

Fig. 8 Measured far-field intensity for the MM and the MMHS waveguide at 650 A/cm^2 for a QCL emitting at a nominal frequency of 2.7 THz. The far-field intensity at Φ = 0° and Θ = 0° is improved by a factor of 4.0. Due to the small reduction of the effective index, the beam collimation is not affected for the given MMHS parameters

Interestingly, the field distribution in Fig. 5d (for a frequency of 2.9 THz) is much stronger near the facet than the field distribution in Fig. 5b (for a frequency of 1.45 THz) even though the total efficiency at 1.45 THz is greater than the total efficiency at 2.9 THz. However, tightly confined field distributions in the near-field will be composed of non-propagating evanescent waves. Propagating waves will have lower spatial frequencies that will be less visible. This can be seen in Fig. 6 where the absolute value of the electric field $|E_z|$ (for the frequencies in Fig. 5b–d) is plotted as a function of the propagation distance. According to Fig. 6a, the present electric near field in Fig. 5d is attributed to a predominantly evanescent wave, since the index contrast is quiet high. Since the main laser emission takes place on the top of the facet of the QCL, the electric field E_z is also plotted for a corresponding z position in Fig. 6b.

In addition, the far-field at a frequency of 1.7 THz, where the total out-coupling efficiency is maximized, is presented in Fig. 7. The improved simulated collimation for the MMHS waveguide in horizontal direction Fig. 7a–b is illustrated in Fig. 7c for a set horizontal direction $\Phi = 0°$. The beam pattern is both more centered and symmetric in vertical direction.

Finally, the far-field for both the MM and the MMHS waveguide is presented in Fig. 8 for a current density of 650 A/cm^2. The far-field intensity at $\Phi = 0°$ and $\Theta = 0°$ is improved by factor of 4. This is due to the improved waveguide impedance matching and constructive interference. However, a significant change in the beam collimation is not observed. This can be explained by the relatively small reduction of the effective refractive index of the MMHS waveguide ($n_{eff} = 3.16$) with respect to the MM waveguide ($n_{eff} = 3.5$) which is only 11 %. In contrast, for larger reductions of the effective index (for example at 1.7 THz), there is an improvement in the beam collimation as shown in Fig. 7. Interference fringes [5, 28] are not observed, since the profile is measured in central emission direction where no fringes occur. Also, the sample mount design blocks the emission from the back facet.

In conclusion, by FIB-milling, sub-wavelength metal lines on the top layer of a MM waveguide a hybrid section has been formed, where the lasing mode can penetrate into air. The hybrid section is found to improve significantly the out-coupling efficiency of the MM waveguide, and in contrast to other schemes, the approach presented here is straightforward to implement. Although a FIB was used to define the lines in this work, photo-lithography could be used instead. In addition, FDTD simulations show that an almost ideal out-coupling performance of about 87 % can be achieved, if a balanced reflection minimization is employed.

Acknowledgments The work was financially supported by Referat 221 MIWF NRW, BMBF Quantum communication program—Q.com-H 16KIS0109 and BMBF-QUIMP 16BQ1062 as well as Mercur Pr-2013-0001. We are also grateful for the support from the EPSRC (UK), the ERC TOSCA program, the Royal Society, and the Wolfson Foundation. The authors would also like to acknowledge the DFH/UFA CDFA-05-06 Nice-Bochum and the RUB Research School. Additionally, T.F, S.P, N.J., and A.D.W. would like to acknowledge IMPRS-SurMat, MPIE Düsseldorf. T.F., S.M., and N.J. would like to acknowledge DFG GSC 98/3 RUB Research School PLUS.

References

1. R. Köhler, A. Tredicucci, F. Beltram, H. E. Beere, E. H. Linfield, A. G. Davies, D. A. Ritchie, R. C. Iotti, and F. Rossi, Nature 417, 156 (2002).
2. S. Fathololoumi, E. Dupont, C. Chan, Z. Wasilewski, S. Laframboise, D. Ban, A. Mtys, C. Jirauschek, Q. Hu, and H. C. Liu, Optics Express 20, 3866 (2012).

3. B. S. Williams, S. Kumar, H. Callebaut, Q. Hu, and J. L. Reno, Applied Physics Letters 83, 2124 (2003).
4. S. Kohen, B. S. Williams, and Q. Hu, Journal of Applied Physics 97, 053106 (2005).
5. A. J. L. Adam, I. Kaalynas, J. N. Hovenier, T. O. Klaassen, J. R. Gao, E. E. Orlova, B. S. Williams, S. Kumar, Q. Hu, and J. L. Reno, Applied Physics Letters 88, 151105 (2006).
6. B. S. Williams, S. Kumar, Q. Hu, and J. L. Reno, Electronics Letters 42, 89 (2006).
7. L. Li, L. Chen, J. Zhu, J. Freeman, P. Dean, A. Valavanis, A. G. Davies, and E. H. Linfield, Electronics Letters 50, 309 (2014).
8. L. H. Li, J. X. Zhu, L. Chen, A. G. Davies, and E. H. Linfield, Optics Express 23, 2720 (2015).
9. M. Brandstetter, C. Deutsch, M. Krall, H. Detz, D. C. MacFarland, T. Zederbauer, A. M. Andrews, W. Schrenk, G. Strasser, and K. Unterrainer, Applied Physics Letters 103, 171113 (2013).
10. D. Turcinkova, M. I. Amanti, G. Scalari, M. Beck, and J. Faist, Applied Physics Letters 106, 131107 (2015).
11. M. I. Amanti, M. Fischer, G. Scalari, M. Beck, and J. Faist, Nature Photonics 3, 586 (2009).
12. G. Xu, R. Colombelli, S. P. Khanna, A. Belarouci, X. Letartre, L. Li, E. H. Linfield, A. G. Davies, H. E. Beere, and D. A. Ritchie, Nature Communications 3, 952 (2012).
13. Y. Chassagneux, R. Colombelli, W. Maineult, S. Barbieri, H. E. Beere, D. A. Ritchie, S. P. Khanna, E. H. Linfield, and A. G. Davies, Nature 457, 174 (2009).
14. A. Wei Min Lee, Q. Qin, S. Kumar, B. S. Williams, Q. Hu, and J. L. Reno, Optics letters 32, 2840 (2007).
15. R. Degl'Innocenti, Y. D. Shah, D. S. Jessop, Y. Ren, O. Mitrofanov, H. E. Beere, and D. A. Ritchie, Optics Express 22, 24439 (2014).
16. A. A. Tavallaee, P. W. C. Hon, K. Mehta, T. Itoh, and B. S. Williams, IEEE Journal of Quantum Electronics 46, 1091 (2010).
17. P. W. C. Hon, A. A. Tavallaee, Q.-S. Chen, B. S. Williams, and T. Itoh, IEEE Transactions on Terahertz Science and Technology 2, 323 (2012).
18. N. Yu, Q. J. Wang, M. A. Kats, J. A. Fan, S. P. Khanna, L. Li, A. G. Davies, E. H. Linfield, and F. Capasso, Nature Materials 9, 730 (2010).
19. G. Liang, E. Dupont, S. Fathololoumi, Z. R. Wasilewski, D. Ban, H. K. Liang, Y. Zhang, S. F. Yu, L. H. Li, A. G. Davies, E. H. Linfield, H. C. Liu, and Q. J. Wang, Scientific Reports 4 (2014).
20. M. I. Amanti, M. Fischer, C. Walther, G. Scalari, and J. Faist, Electronics Letters 43, 573 (2007).
21. W. Maineult, P. Gellie, A. Andronico, P. Filloux, G. Leo, C. Sirtori, S. Barbieri, E. Peytavit, T. Akalin, J.-F. Lampin, H. E. Beere, and D. A. Ritchie, Applied Physics Letters 93, 183508 (2008).
22. A. Brewer, J. R. Freeman, P. Cavali, J. Maysonnave, J. Tignon, S. S. Dhillon, H. E. Beere, and D. A. Ritchie, Applied Physics Letters 104, 081107 (2014).
23. F. Castellano, L. Li, E. H. Linfield, A. G. Davies, H. E. Beere, D. A. Ritchie, and M. S. Vitiello, Optics Express 23, 5190 (2015).
24. R. Degl'Innocenti, Y. D. Shah, R. Wallis, A. Klimont, Y. Ren, D. S. Jessop, H. E. Beere, and D. A. Ritchie, Applied Physics Letters 106, 082101 (2015).
25. M. I. Amanti, G. Scalari, R. Terazzi, M. Fischer, M. Beck, J. Faist, A. Rudra, P. Gallo, and E. Kapon, New Journal of Physics 11, 125022 (2009).
26. M. Brandstetter, M. Krall, C. Deutsch, H. Detz, A. M. Andrews, W. Schrenk, G. Strasser, and K. Unterrainer, Applied Physics Letters 102, 231121 (2013).
27. J. B. Khurgin, Optics Express 23, 131107 (2015).
28. M. Brandstetter, C. Deutsch, A. Benz, G. Cole, H. Detz, A. M. Andrews, W. Schrenk, G. Strasser, and K. Unterrainer Optics Express 20. 23832 (23833).